




Article

Photocatalytic and Electrochemical Activity of Magnesium Oxide Nanoballs Synthesized via a Hydrothermal Route

Suresh Sagadevan ^{1,*}, J. Anita Lett ², Is Fatimah ³ , K. Tamizh Selvi ⁴, Ramesh Poonchi Sivasankaran ⁵, Getu Kassegn Weldegebrail ⁶  and Won-Chun Oh ^{7,*} 

- ¹ Nanotechnology & Catalysis Research Centre, University of Malaya, Kuala Lumpur 50603, Malaysia
 - ² Department of Physics, Sathyabama Institute of Science and Technology, Chennai 600119, India
 - ³ Department of Chemistry, Faculty of Mathematics and Natural Sciences, Universitas Islam Indonesia, Kampus Terpadu UII, Jl. Kaliurang Km 14, Sleman, Yogyakarta 55584, Indonesia
 - ⁴ Department of Physics, Vel Tech High Tech Rangarajan Sakunthala Engineering College, Chennai 600062, India
 - ⁵ Environmental and Climate Technology, Korea Institute of Energy Technology (KENTECH), 200 Hyeoksins-ro, Naju 34129, Korea
 - ⁶ Department of Chemistry, College of Natural and Computational Sciences, Debre Berhan University, Debre Berhan P.O. Box 445, Ethiopia
 - ⁷ Department of Advanced Materials Science and Engineering, Hanseo University, Seosan-si 31962, Korea
- * Correspondence: drsureshnano@gmail.com (S.S.); wc_oh@hanseo.ac.kr (W.-C.O.)

Abstract: Currently, there is growing concern about minimizing the environmental impacts caused by the generation of waste on water, soil, air pollution, and contamination of the environment in general. Magnesium oxide (MgO) nanoballs (NBs) were synthesized by the hydrothermal method followed by a calcination process. The average size of particles dispersed in deionized water was 159.2 ± 70 nm. The energy band gap was calculated to be 5.14 eV. The magnetic behavior, cyclic voltammetry, and electrochemical impedance of MgO NBs were studied. Under visible-light irradiation, the photocatalytic activity of MgO nanoballs was investigated by methylene blue (MB) dye. Results showed that photodegradation for MB under visible light irradiation for 120 min and degradation results are fitted well with pseudo-first-order reaction kinetics with a rate constant of 0.00252 min^{-1} and a correlation coefficient of 0.96.

Keywords: MgO nanostructures; hydrothermal synthesis; optical properties; electrochemical property; photocatalytic activity



Citation: Sagadevan, S.; Lett, J.A.; Fatimah, I.; Selvi, K.T.; Sivasankaran, R.P.; Weldegebrail, G.K.; Oh, W.-C. Photocatalytic and Electrochemical Activity of Magnesium Oxide Nanoballs Synthesized via a Hydrothermal Route. *Processes* **2022**, *10*, 2098. <https://doi.org/10.3390/pr10102098>

Academic Editor: Aneta Magdziarz

Received: 14 August 2022

Accepted: 13 October 2022

Published: 17 October 2022

Publisher's Note: MDPI stays neutral with regard to jurisdictional claims in published maps and institutional affiliations.



Copyright: © 2022 by the authors. Licensee MDPI, Basel, Switzerland. This article is an open access article distributed under the terms and conditions of the Creative Commons Attribution (CC BY) license (<https://creativecommons.org/licenses/by/4.0/>).

1. Introduction

Nanotechnology is an emerging field of science that is gaining popularity in the worldwide due to its potential applications in fields such as medicine, automotives, and the environment [1,2]. Nanotechnology is also inevitable due to increased versatility in production with desired size and morphology for a variety of applications such as sensors, automotive spare parts processing and drug delivery [3,4]. Nanomaterials have enhanced physicochemical properties and intensified efficiency-enhancing activities in a variety of applications including wastewater treatment, biomedical, optical, sensory, antibacterial and electrochemical applications [5,6]. Advances in industrialization resulting in toxic by-products have altered the environment, releasing a certain variety of toxins and emissions of hazardous gases into the atmosphere. In this regard, traditional methods such as immobilization, biological and chemical oxidation, and incineration have been widely used to treat a variety of organic and toxic industrial pollutants [7]. Various physical, chemical, and biological processes are used to remove colorants and other hazardous contaminants from wastewater [8]. Some physical and chemical treatment methods such as coagulation, precipitation, flocculation, ion exchange, membrane filtration, and adsorption techniques are commonly used to remove contaminants, although they are not optimal for complete

contaminant removal [9]. Heterogeneous photocatalysis using semiconductor oxides has been used to mineralize organic impurities into H_2O , CO_2 and inorganic ions [10]. Due to solar energy, photocatalysis in water treatment has an excellent position compared to other conventional approaches [11]. Nanomaterials have unique chemical and physical properties, such as larger surface areas and surface defects [12]. It would also be used in photocatalytic degradation [10,13]. The optical properties of nanomaterials are mainly influenced by their size and shape [14]. Compared to metal oxides, nanostructures are environmentally friendly, exhibit high mobility and chemical and thermal stability, have low cost, show compatibility, and involve a simple process. In the class of metal oxide nanostructures, MgO has attracted much attention due to its unique biocompatibility and extreme stability [15,16]. The MgO nanostructure has been considered for various applications including electronics, catalysis, additives, ceramics, photochemical products, paints and medicine [17,18]. Numerous techniques are used to produce MgO nanoballs, such as sol-gel, hydrothermal, spray pyrolysis, combustion, microwave, and co-precipitation methods [19–25].

Metal oxide nanostructures are widely characterized by their effective photocatalysts in water treatment processes, including pharmaceutical and dye-containing effluents [26–29]. Because of these intriguing properties, scientists have experimented with a variety of metal oxides to improve the efficiency of nanomaterials. MgO nanomaterials have been explored as a non-toxic and environmentally friendly adsorbent to remove organic pollutants and toxic metal ions from water [30]. The dye contaminants discharged from dye industries are chemically stable, and common physical, chemical, and biological methods for removing toxic dyes from wastewater, such as adsorption, coagulation, gentrification, filtration, and reverse osmosis, are ineffective [31,32]. For the decomposition of toxic compounds in wastewater, advanced oxidation processes such as sonic catalysis, ozone decomposition, photo Fenton, photocatalysis, and photo electro-Fenton have become popular [33,34]. Depending on the source of the dyes and the remediation methods, each method has advantages and disadvantages. The technique associated with UV radiation and hydroxide oxidation does not effectively treat color dyes either. The photocatalytic method has recently received a lot of attention due to its effective dye decolorization [35,36]. In a photocatalytic reaction, the semiconductor material absorbs energy equal to the band gap and generates electric charges, resulting in an oxidation and reduction reaction that leads to dye degradation [37]. Methylene blue is a cationic thiazine dye that is commonly used in the paper and textile industries for dyeing and printing. Therefore, in this work, MgO nanoballs are synthesized via a hydrothermal route, and their electrochemical impedance, cyclic voltammetry and photocatalytic activity are investigated.

2. Materials and Methods

2.1. Materials

MgO nanoballs were formed by the hydrothermal synthesis route of magnesium nitrate ($Mg(NO_3)_2 \cdot 6H_2O$), in the presence of sodium hydroxide (NaOH) (purchased from Sigma-Aldrich, Mumbai, India) and PVA. All chemicals and solvents used during the synthesis were analytical-grade reagents and used as received without any further purification.

2.2. Synthesis of MgO Nanoballs

In this work, MgO NBs were prepared by a hydrothermal method followed by a calcination process. In a typical synthesis, 0.5 M magnesium nitrate ($Mg(NO_3)_2 \cdot 6H_2O$) was added to 50 mL of double distilled water and stirred well for 30 min. Then, 2 g NaOH and 4.3 g PVA were added directly to the above solution. The resulting homogeneous mixture was transferred to a Teflon-lined autoclave. The autoclave was sealed and subjected to a temperature of 180 °C for 12 h and then cooled to room temperature. On cooling, the precipitate formed was filtered, washed with distilled water to remove excess residual ions, and then washed with ethanol. Subsequently, the precipitate was dried in an oven at 80 °C

for 4 h to obtain the $\text{Mg}(\text{OH})_2$. In order to convert the amorphous phase of $\text{Mg}(\text{OH})_2$ to MgO , the samples were calcined at 350°C for 2 h under the air atmosphere.

2.3. Photocatalytic Activity Study

The photocatalytic reactor comprises a 250 W Xenon lamp that serves as a visible-light source. To examine the photocatalytic activity of the synthesized sample on the dye, 40 mg of the catalyst was placed in a 250 mL beaker containing 80 mL of 15 ppm MB dye and stirred for 30 min in a dark room to induce the adsorption/establish desorption equilibrium. The process of the photodegradation was followed by observing the change in the absorption maximum wavelength of 664 nm of the dye. The percentage of degradation (Degradation (%)) of the MB dye was calculated using Equation (1):

$$\text{Degradation}(\%) = (1 - A/A_0) \times 100 \quad (1)$$

where A and A_0 represent the absorbance of MB dye before and after exposure to visible-light irradiation, respectively.

2.4. Electrochemical Measurement

The electrochemical measurement was carried out on a three-electrode system. GCE/MgO NBs, platinum wire, and Ag/AgCl were used as working, counter and reference electrodes, respectively. 0.5 M Na_2SO_4 solution was used as an electrolyte throughout the experiment in the potential window between -1.1 to 1.8 V with a scan rate of 20 mV/s. The catalyst sample was prepared by dispersing it in ethanol. The working electrode was fabricated by first cleaning the surface of the glassy carbon electrode (GCE) with alumina and then drop casting the $15\ \mu\text{L}$ of the as-synthesized MgO sample on it and kept for dry. Electrochemical impedance measurement was performed by a Versa STAT MC impedance spectrometer in the frequency range from 1 Hz to 1 MHz at room temperature.

2.5. Characterisation

The X-ray diffractometer (PANalytical, X'Pert) was used with $\text{CuK}\alpha$ radiation ($\lambda = 1.5406\ \text{\AA}$) in the range of 10 – 70° . The presence of functional molecules in the synthesized MgO NBs was confirmed by Fourier Transform Infrared spectroscopy (FTIR) (Perkin Elmer, Waltham, MA, USA). The surface morphological analysis of MgO NBs was performed using scanning electron microscopy (FEI-Quanta FEG 200F instrument) (Hillsboro, OR, USA). The Varian, Cary 5000 spectrophotometer was used to examine the UV-Vis spectrum of MgO NBs between 300 and 800 nm. Photoluminescence spectra (PL) were recorded using FLUOROLOG—FL3—11 Jobin Yuvo make Spectro-fluorometer (Edison, NJ, USA). The Lakeshore VSM7410 magnetometer provides the M-H hysteresis loop for MgO NBs.

3. Results and Discussion

3.1. X-ray Diffraction Analysis

Figure 1a represents the XRD pattern of MgO nanoballs, which reveals the characteristic peak with the planes of $(1\ 1\ 1)$, $(2\ 0\ 0)$, and $(2\ 2\ 0)$. These planes match well with (JCPDS No. 87-0653) with a cubic crystal system. The most intense and characteristic peak among all XRD patterns corresponds to the reflecting plane $(2\ 0\ 0)$, showing the formation of a single-phase cubic structure. Additionally, as provided in the figure, the diffraction patterns formed are high sharp, narrow, and with significant intensity where all these factors support the crystalline nature of the formed MgO NBs. The crystalline size (D) of MgO was calculated using the Debye–Scherrer formula given below:

$$D = 0.94\lambda / \beta \cos \theta \quad (2)$$

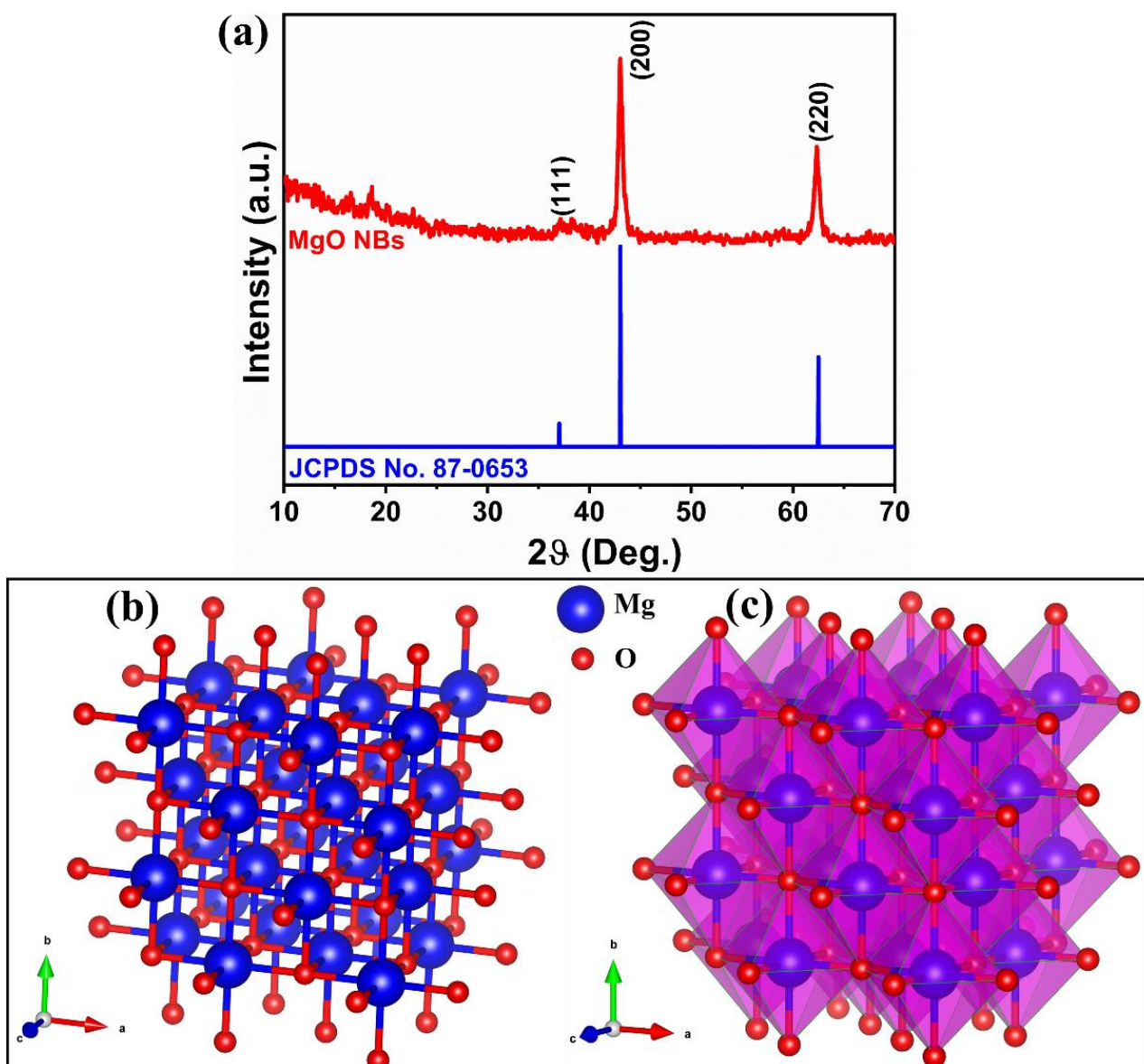


Figure 1. (a) Powder XRD pattern of MgO NBs. The cubic crystal structure of MgO drawn by Vesta software (Version 3.4.5); (b) Ball-and-stick model and (c) Polyhedral model. Unit cell lattice parameters: crystal system—Cubic, space group—Fm-3m, distances $a = b = c = 4.21700$, along with axes (for Mg, $x = 0$, $y = 0$ and $z = 0$ and for O, $x = 0.500000$, $y = 0.500000$ and $z = 0.500000$), and angles $\alpha = \beta = \gamma = 90^\circ$.

The mean crystallite size of MgO nanoballs was found to be 14 nm. D is the average crystallite size, θ is Bragg's diffraction angle, λ (1.540 Å) is the wavelength of the X-ray source, and β is full width at half maximum (FWHM). Moreover, Figure 1b,c shows the ball-and-stick model and polyhedral model of MgO, respectively, where it can be seen that arrangement of Mg²⁺ and O²⁻ ions in the MgO crystal structure. These two representations demonstrated that each O²⁻ anion is octahedrally coordinated by six Mg²⁺ cations, while each Mg²⁺ cation is octahedrally coordinated by six O²⁻ anions.

3.2. FTIR Analysis

Fourier transform-infrared spectroscopy in transmission mode was utilized to generate the spectra for obtaining the information about compounds present on MgO nanoballs. Figure 2 shows the FTIR spectrum of MgO NBs. The FT-IR spectra of MgO NBs exhibited broad peak at 3456 cm⁻¹ assigned to the -OH stretching vibration of water molecules. The

sharp and high intense peak at 3696 cm^{-1} indicates the presence of surface hydroxyl group on the crystal face of low-coordination sites or defect sites [38]. The weak peak existed at 1638 cm^{-1} corresponds to the bending vibration of the surface hydroxyl group [38]. The characteristic peak was observed at 501 cm^{-1} corresponding to the stretching mode of Mg-O bond. The strong bands at 1389 and 839 cm^{-1} were assigned to carbonate species (CO_3^{2-}) chemisorbed on the surface of MgO NBs [39]. In addition, a weak band observed at 2442 cm^{-1} belongs to the adsorption of gas phase CO_2 molecules [40]. The weak peak at 2756 cm^{-1} could be assigned to the -C-H stretching vibration of residual PVA [41]. Furthermore, no impurities were found. The IR spectrum confirmed the pure cubic crystal structure of the MgO samples prepared. Hence, it is known that these generated functional groups on the surface of MgO nanoballs play an important role in the catalytic reaction.

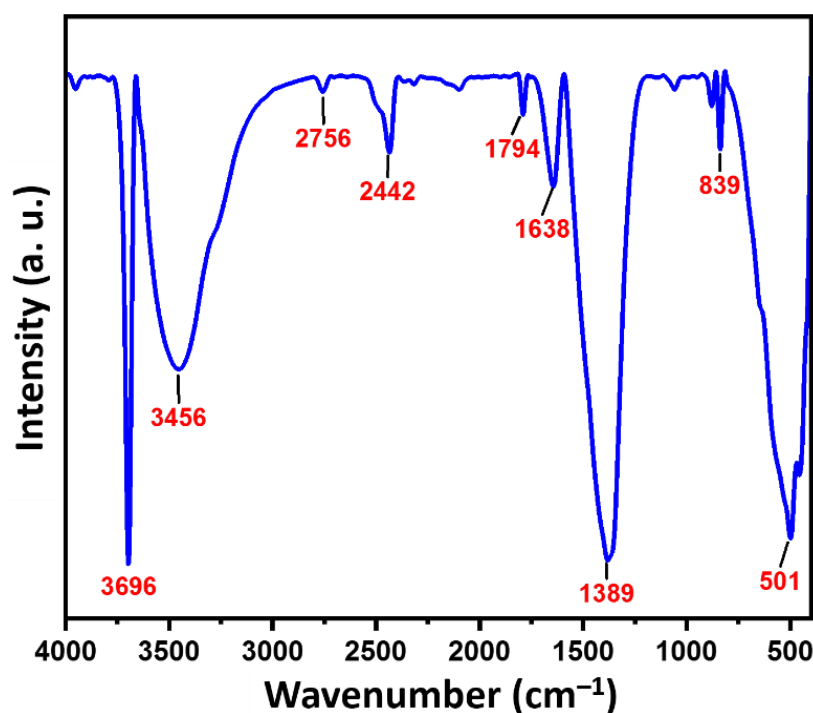


Figure 2. FTIR spectrum of MgO NBs.

3.3. Morphology

Figure 3a–d shows that the SEM images of MgO NBs at different magnifications, where it can be clearly seen that the MgO NPs have rough surface and nanoballs morphology. The agglomeration among NBs was enhanced. Due to the high surface charge and high magnetization among nanoballs, agglomeration occurred. Furthermore, the elemental analysis of MgO NBs as shown in Figure 3e, EDX confirms the presence of Mg and O elements in the sample. Figure 4 shows the EDS elemental mapping of MgO NBs. The mapping was derived from SEM image to analyze elemental distribution. The combined elemental distribution ensures a homogeneous distribution of all elements in the MgO NBs (Figure 4b). The red color represents the presence of oxygen in MgO NBs (Figure 4c). The green color in Figure 4d confirms the presence of magnesium in MgO NBs.

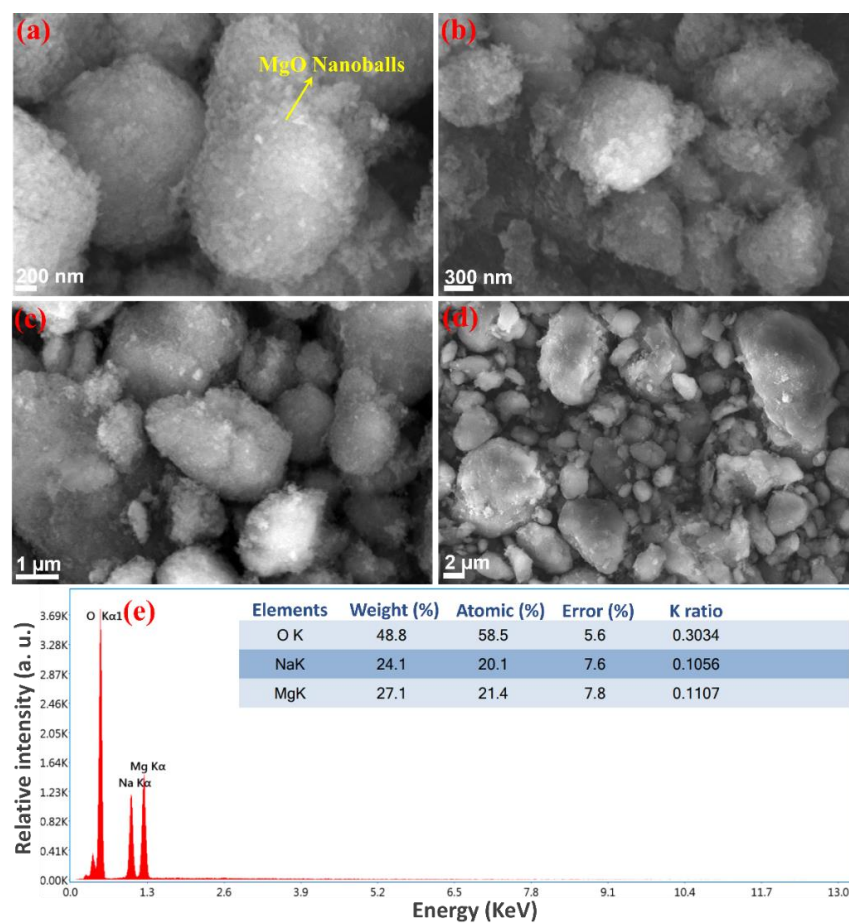


Figure 3. SEM images at different magnifications (a–d) and EDX spectrum (e) of MgO NBs.

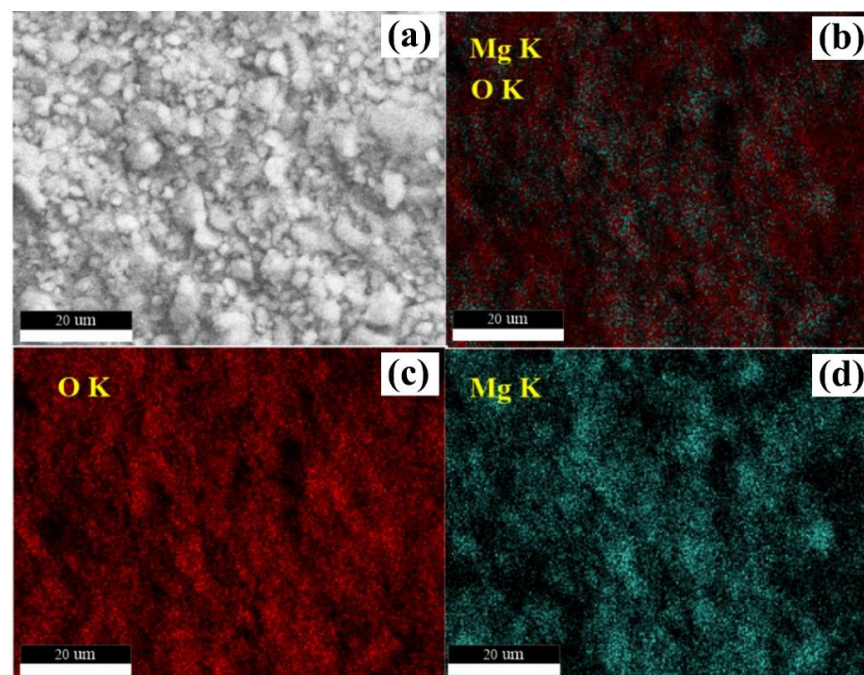


Figure 4. EDS mapping of MgO NBs. (a) SEM micrograph of MgO NBs, (b) elemental distribution of Mg and O, (c) distribution of O elements and (d) distribution of Mg elements.

3.4. Dynamic Light Scattering

The dynamic light scattering (DLS) particle size analyzer was used to confirm the size and distribution of the MgO NBs. The plot of differential intensity as a function of diameter (nm) is shown in Figure 5. From the figure given in the histogram, the average hydrodynamic diameter of the MgO particles in water is 159.2 ± 70 nm.

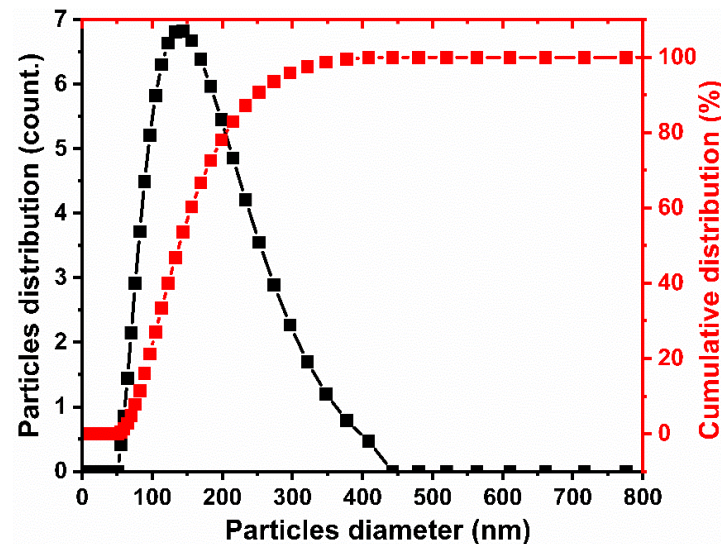


Figure 5. DLS spectrum of the MgO NBs.

3.5. Optical Properties

The optical properties of MgO NBs have analyzed the determination of the electronic transitions type and bandgap. The UV–Vis absorbance spectrum of MgO NBs in the range of 200–800 nm is shown in Figure 6a. As can be seen from the figure, the maximum absorption occurs at 280 nm. The absorption at 280 nm is attributed to the coordination of surface oxide ions, with the associated high wavelength of the surface exciton indicating low coordination. The band gap energies were calculated by extrapolating the line from the Kubelka–Munk function $F(R)$ graph versus photon energy as shown in Figure 6b. The bandgap of the MgO NBs was estimated to be 5.14 eV. is in good agreement with the earlier report [42,43]. MgO is a wide and direct gap semiconductor as evidenced from the above results and there is a red shift in bandgap from the bulk (7.65 eV) [43]. The redshift can be explained based on various main active facets and excitation energies and also due to the quantum size effect [43].

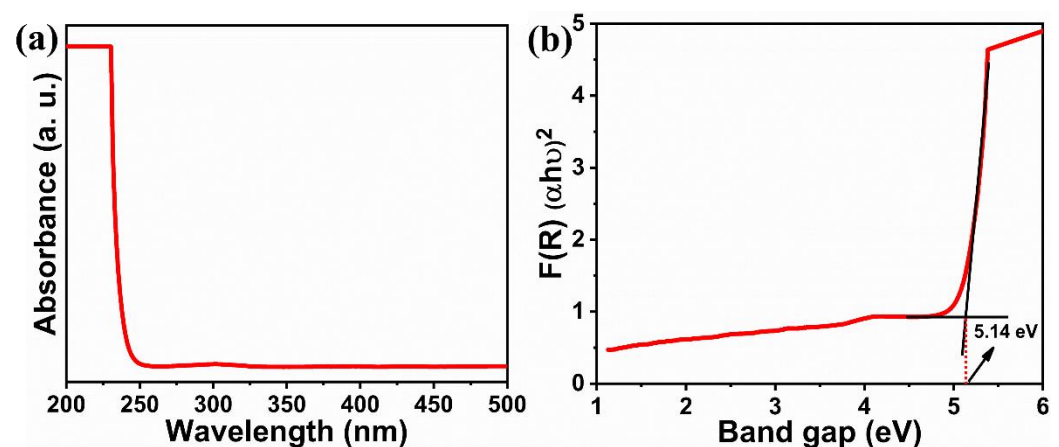


Figure 6. UV–Vis absorbance spectrum (a,b) determination of the band gap energy by the Kubelka–Munk function.

3.6. PL Spectra

Figure 7 shows the PL spectrum of MgO NBs. The strong UV emission peak at 362 nm can be seen in the PL spectrum due to the direct recombination of holes and electrons in the energy band. The visible emission band at 443 nm is caused by oxygen vacancies, Mg vacancies, or Mg interstitials [44], which induce new energy levels in the band gap of MgO. The most common defects in nanomaterials, oxygen vacancies, cause lattice distortions in their immediate vicinity and act as a radiative center in luminescence processes. The MgO NBs have a larger surface area with an oxygen defect on the surface, making them excellent photocatalysts.

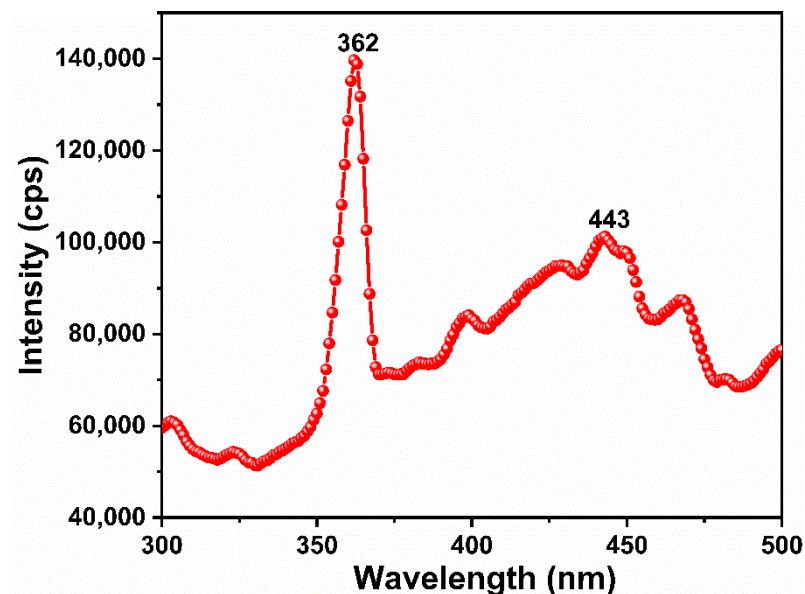


Figure 7. PL spectrum of MgO NBs.

3.7. Magnetic Studies

Figure 8 shows the magnetization curve at room temperature. Studying the magnetic properties of a material is crucial as it provides insight into the observed defects, imperfections, structural changes, and electron configurations. In the low range of the applied magnetic field, the MgO NBs show diamagnetism and small ferromagnetic behavior, as shown in Figure 8. In the low-frequency range, the MgO nanoplates appear to be ferromagnetic. Defects such as oxygen vacancies, Mg vacancies, and dangling bonds were thought to be responsible for the ferromagnetism of the MgO NBs. Many research groups have dealt with defect-induced magnetism (DIM). Ferromagnetism is highly defective in MgO NBs at room temperature. MgO is non-magnetic in bulk but ferromagnetic in the nanostructure at room temperature [45]. DIM in MgO NBs is caused by the spin polarization of 2p electrons from oxygen atoms near the Mg vacancies [46]. The calculated susceptibility (χ), remanence (M_r), and magnetic coercivity (H_{ci}) are presented in Table 1. The negative susceptibility value indicates that the MgO nanomaterial is diamagnetic.

Table 1. Calculated value of susceptibility (χ), remanence (M_r), and magnetic coercivity (H_{ci}).

M_r	M_{max}	H_{ci}	$\chi = M/H$
10^{-6} (emu/g)	(emu/g)	(G)	10^{-8} (emu/gG)
17.39	−0.00021989	972.33	−1.4659

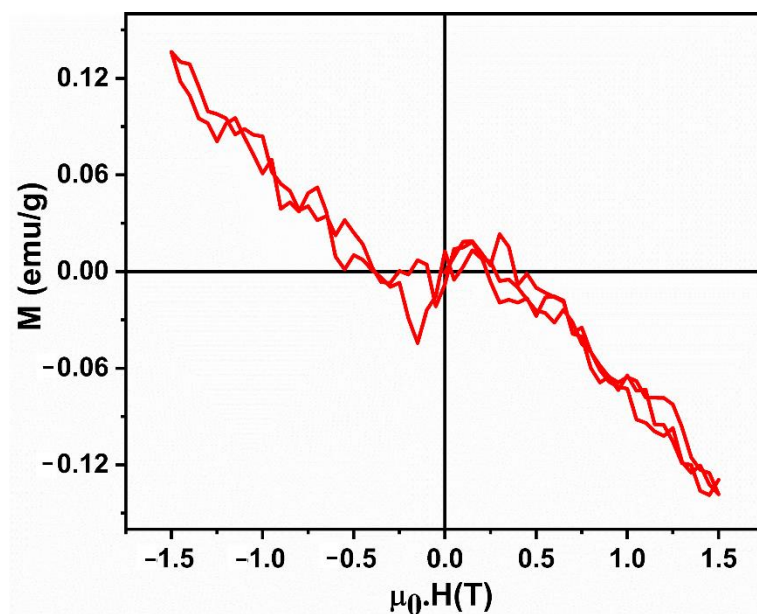


Figure 8. M-H hysteresis loop observed at room temperature.

3.8. Electrochemical Studies

The most common method for determining the oxidation-reduction process of inorganic molecular species by using cyclic voltammetry (CV). The efficiency of charging, discharging and reversibility of the reaction between the electrodes can all be quantified and this is done with CV. Figure 9a shows the results of cyclic voltammetric studies of MgO NBs. The CV curves represent the quasi-reversible electron transfer process, suggesting that the redox mechanism is the cause of the measured capacitance [47]. However, the course of the curve indicates that the characteristic capacitance determined differs from that of an electric double-layer capacitor, which could partially represent an almost rectangular CV curve [48]. Figure 9b shows the Nyquist plots with equivalent circuit diagram for the MgO sample. As shown in Figure 9b, MgO NBs showed a semi-circle in the Nyquist plot, which is ascribed to the direct charge-transfer at the GCE/MgO electrode and electrolyte interface. Figure 9b inset shows the equivalent circuit diagram which contains R_s , R_{ct} , Z_w and CPE as the solution resistance, charge-transfer resistance at the electrode–electrolyte interface, Warburg impedance and constant phase element, respectively.

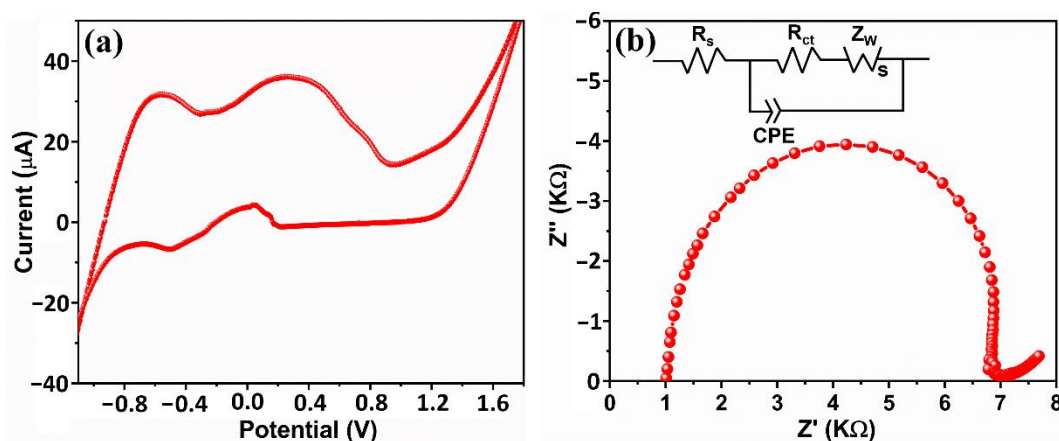


Figure 9. Cyclic voltammetry (a), Nyquist plot (b) of MgO NBs.

3.9. Photocatalytic Activity Study

Photocatalytic tests on the degradation of MB dye were performed in the presence of a catalyst for 120 min. The degradation efficiency of the dyes was determined under visible-light irradiation and at 30-min intervals by exposing a known amount of solution to the UV–Vis spectrometer; the resulting UV–Vis spectra of the dyes are shown in Figure 10a (MB dye). There was a frequent drop in the dye absorption band; as a result, deterioration increased with time. When the solution is illuminated with visible light in the presence of the catalyst, the absorption peaks steadily decrease with irradiation time, demonstrating the increased photocatalytic activity of MgO NBs. During the early stages of the contact time, the decay of the absorption peak for MB was rapid but slowed as the process reached equilibrium. The decrease in the maximum absorption wavelength (λ_{\max}) of the dye with the irradiation time, as shown in Figure 10a,b, indicates the photoactivity of the synthesized sample. Figure 10c was achieved for 2 h of exposure to visible light at pH with the other experimental parameters indicated and without the initial addition of an electron-accepting or -donating species to the reaction medium.

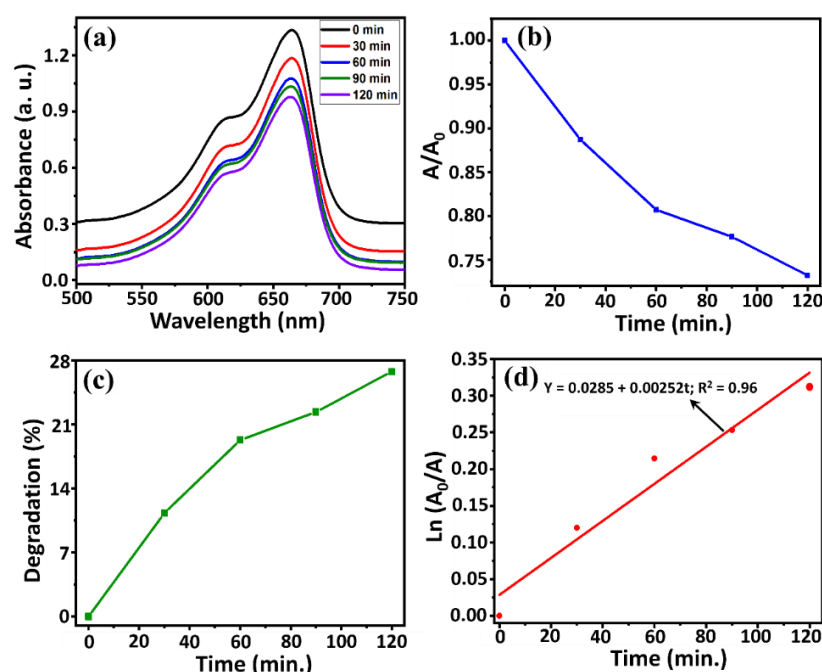


Figure 10. Photodegradation of MB under visible light irradiation; change of absorbance with time (a), change of normalized absorbance with time (b), degradation percentage (c), and kinetics plot (d).

The half-life of the reaction ($t_{1/2}$), the time it takes for the initial concentration of the dye to decrease by half, is shown in Equation (4).

$$\ln(A_0/A) = k_1 t \quad (3)$$

$$t_{1/2} = \ln(2)/k_1 \quad (4)$$

where k_1 refers to the rate constant of the reaction in time t , and A_0 and A are as defined in Equation (1).

The experimental degradation data also fit well with the pseudo-first-order reaction, Equation (4), and graphically illustrated in Figure 10d, with a reaction rate constant of 0.00252 min^{-1} and a coefficient of correlation of 0.96. The photocatalytic activity of metal oxide nanoballs is closely related to their different synthesis conditions, crystallite size, morphology, and surface properties. The concentration of defects on the surface of the nanoballs can also make a difference in the photocatalytic activity. These surface defects act as electron traps to inhibit the recombination between photogenerated electron–hole pairs.

The radical (superoxide and hydroxyl) groups are dynamic to boost the oxidation of organic pollutants. Thus, it is recommended that the oxygen vacancies (luminescence studies) are in favor of photocatalytic reactions. The photocatalytic activity process for MgO under visible-light irradiation. The electrons generated by the CB are transferred to the MgO catalyst where they combine with ambient O₂ to create superoxide radicals. Meanwhile, the holes in the VB react with the H₂O. The superoxide radicals formed during dye activation accelerate the breakdown of the dye molecule [49,50]. Table 2 provides a comparison of the photodegradation performances achieved by MgO nanoparticles synthesized using different methods for various pollutants under different conditions.

Table 2. Comparison of the photocatalytic degradation of dyes using various MgO nanoparticles.

S.No.	Type of Nanocomposites	Synthesis Method	Contaminant (s)	Light	% Removal	Pseudo-First-Order Rate Constant	Reference
1	MgO nanostructures	microwave-assisted	MB	sunlight irradiation	88%	0.02086 min ^{−1}	[42]
2	MgO nanostructures	hydrothermal	MB	sunlight irradiation	92%	0.02611 min ^{−1}	[42]
3	MgO nanostructures	microwave-assisted	CR	sunlight irradiation	82%	0.00851 min ^{−1}	[42]
4	MgO nanostructures	hydrothermal	CR	sunlight irradiation	86%	0.01189 min ^{−1}	[42]
5	MgO Nanoparticles	combustion method	MB	UV irradiation.	75%	-	[51]
6	MgO nano powders	bio mediated route	MG	sunlight irradiation	-	-	[52]
7	MgO nano powders	bio mediated route	MG	UV light	-	-	[52]
8	MgO nano powders	bio mediated route	Rh-B	sunlight irradiation	-	-	[52]
9	MgO nano powders	bio mediated route	Rh-B	UV light	-	-	[52]
10	MgO nano powders		IC dye	UV light irradiation	-	-	[53]
11	MgO Nanoparticles	Green synthesis	MB	ultraviolet (UV)	70%	-	[54]
12	MgO Nanoparticles	sol-gel method	MB	UV irradiation	52%	0.0038 min ^{−1}	[55]
13	MgO Nanoparticles	Hydrothermal synthesis	MB	Visible	27%	0.00252 min ^{−1}	Present work

4. Conclusions

Magnesium oxide has received a lot of attention due to its biocompatibility and stability under extreme conditions. It has been used in various application areas such as electronics, catalysis, additives, ceramics, photochemical products, paints, and medicine. In this present work, MgO NBs are successfully synthesized by the hydrothermal method followed by a calcination process and thoroughly characterized in terms of their crystallinity, morphology, surface functionality, and optical properties. Powder XRD pattern confirms the formation of MgO phase with high crystallinity. SEM micrographs shows the formation of balls morphology, some of them agglomerated into larger particles. FTIR spectra confirms the characteristic stretching vibration of Mg-O bond with some surface-functionalized groups originating from the reaction medium during synthesis and atmospheric moisture. Dynamic light scattering measurements demonstrated the stability of the synthesized MgO NBs in an aqueous media with an average hydrodynamic diameter of 159.2 nm. Finally, as synthesized MgO nanoballs showed photoactivity towards the degradation of MB under visible light at natural pH and without the initial addition of an electron-accepting or -donating species to the reaction medium.

Author Contributions: S.S.: Conceptualization, Methodology, Formal analysis, Data curation, Validation, Writing—original draft. J.A.L.: Methodology, Formal analysis, Data curation, Visualization,

Validation. I.F.: Formal analysis, Visualization, Data curation. K.T.S.: Investigation, Formal analysis, Validation. R.P.S.: Formal analysis, Data curation, Visualization and Validation. G.K.W.: Investigation, Formal analysis, Data curation, Visualization. W.-C.O.: funding acquisition. All authors have read and agreed to the published version of the manuscript.

Funding: This research received no external funding.

Data Availability Statement: Not applicable.

Conflicts of Interest: The authors declare no conflict of interest.

References

- Subhan, M.A.; Choudhury, K.P.; Neogi, N. Advances with Molecular Nanomaterials in Industrial Manufacturing Applications. *Nanomanufacturing* **2021**, *1*, 75–97. [\[CrossRef\]](#)
- Anita Lett, J.; Sagadevan, S.; Weldegebriale, G.K.; Fatimah, I. Hydrothermal Synthesis and Photocatalytic Activity of NiO Nanoparticles under Visible Light Illumination. *Bull. Chem. React. Eng. Catal.* **2022**, *17*, 340–349. [\[CrossRef\]](#)
- Pradeev Raj, K.; Sadaiyandi, K.; Kennedy, A.; Sagadevan, S. Photocatalytic and antibacterial studies of indium-doped ZnO nanoparticles synthesized by co-precipitation technique. *J. Mater. Sci. Mater. Electron.* **2017**, *28*, 19025–19037. [\[CrossRef\]](#)
- Tharani, K.; Jegatha, C.A.; Sagadevan, S.; Nehru, L.C. Photocatalytic and antibacterial performance of iron oxide nanoparticles formed by the combustion method. *Chem. Phys. Lett.* **2021**, *771*, 138524. [\[CrossRef\]](#)
- Harish, V.; Tewari, D.; Gaur, M.; Yadav, A.B.; Swaroop, S.; Bechelany, M.; Barhoum, A. Review on Nanoparticles and Nanostructured Materials: Bioimaging, Biosensing, Drug Delivery, Tissue Engineering, Antimicrobial, and Agro-Food Applications. *Nanomaterials* **2022**, *12*, 457. [\[CrossRef\]](#)
- Fatimah, I.; Purwiandono, G.; Jauhari, M.H.; Maharani, A.A.A.P.; Sagadevan, S.; Oh, W.-C.; Doong, R.-A. Synthesis and control of the morphology of SnO₂ nanoparticles via various concentrations of *Tinospora cordifolia* stem extract and reduction methods. *Arab. J. Chem.* **2022**, *15*, 103738. [\[CrossRef\]](#)
- Younas, F.; Mustafa, A.; Farooqi, Z.U.R.; Wang, X.; Younas, S.; Mohy-Ud-Din, W.; Ashir Hameed, M.; Mohsin Abrar, M.; Maitlo, A.A.; Noreen, S.; et al. Current and Emerging Adsorbent Technologies for Wastewater Treatment: Trends, Limitations, and Environmental Implications. *Water* **2021**, *13*, 215. [\[CrossRef\]](#)
- Piaskowski, K.; Świdorska-Dąbrowska, R.; Zarzycki, P.K. Dye Removal from Water and Wastewater Using Various Physical, Chemical, and Biological Processes. *J. AOAC Int.* **2018**, *101*, 1371–1384. [\[CrossRef\]](#)
- Qasem, N.A.A.; Mohammed, R.H.; Lawal, D.U. Removal of heavy metal ions from wastewater: A comprehensive and critical review. *Npj Clean Water* **2021**, *4*, 36. [\[CrossRef\]](#)
- Sibhatu, A.K.; Weldegebriale, G.K.; Sagadevan, S.; Tran, N.N.; Hessel, V. Photocatalytic activity of CuO nanoparticles for organic and inorganic pollutants removal in wastewater remediation. *Chemosphere* **2022**, *300*, 134623. [\[CrossRef\]](#)
- EL-Mekkawi, D.M.; Abdelwahab, N.A.; Mohamed, W.A.; Taha, N.A.; Abdel-Mottaleb, M.S. Solar photocatalytic treatment of industrial wastewater utilizing recycled polymeric disposals as TiO₂ supports. *J. Clean. Prod.* **2020**, *249*, 119430.
- Fatimah, I.; Purwiandono, G.; Citradewi, P.W.; Sagadevan, S.; Oh, W.-C.; Doong, R.-A. Influencing Factors in the Synthesis of Photoactive Nanocomposites of ZnO/SiO₂-Porous Heterostructures from Montmorillonite and the Study for Methyl Violet Photodegradation. *Nanomaterials* **2021**, *11*, 3427. [\[CrossRef\]](#)
- Qutub, N.; Singh, P.; Sabir, S.; Sagadevan, S.; Oh, W. Enhanced photocatalytic degradation of Acid Blue dye using CdS/TiO₂ nanocomposite. *Sci. Rep.* **2022**, *12*, 5759. [\[CrossRef\]](#)
- Bai, N.; Kammakakam, I.; Falath, W. Nanomaterials: A review of synthesis methods, properties, recent progress, and challenges. *Mater. Adv.* **2021**, *2*, 1821–1871.
- Ramanujam, K.; Sundrarajan, M. Antibacterial effects of biosynthesized MgO nanoparticles using an ethanolic fruit extract of *Emblica officinalis*. *J. Photochem. Photobiol. B Biol.* **2014**, *141*, 296–300. [\[CrossRef\]](#) [\[PubMed\]](#)
- Jain, A.; Wadhawan, S.; Kumar, V.; Mehta, S. Colorimetric sensing of Fe³⁺ ions in aqueous solution using Magnesium oxide nanoparticles synthesized using green approach. *Chem. Phys. Lett.* **2018**, *706*, 53–61. [\[CrossRef\]](#)
- Salem, J.K.; El-Nahhal, I.M.; Hammad, T.M.; Kuhn, S.; Sharekh, S.A.; El-Askalani, M.; Rolf, H. Optical and fluorescence properties of MgO nanoparticles in micellar solution of hydroxyethyl laurdimonium chloride. *Chem. Phys. Lett.* **2015**, *636*, 26–30. [\[CrossRef\]](#)
- Mangalampalli, B.; Dumala, N.; Grover, P. Allium cepa root tip assay in assessment of toxicity of magnesium oxide nanoparticles and microparticles. *J. Environ. Sci.* **2018**, *66*, 125–137. [\[CrossRef\]](#)
- Shukla, S.K.; Parashar, G.K.; Mishra, A.P.; Misra, P.; Yadav, B.C.; Shukla, R.K.; Bali, L.M.; Dubey, G.C. Nano-like magnesium oxide films and its significance in optical fiber humidity sensor. *Sens. Actuators B* **2004**, *98*, 5–11. [\[CrossRef\]](#)
- Camtakan, Z.; Erenturk, S.; Yusan, S. Magnesium oxide nanoparticles: Preparation, characterization, and uranium sorption properties. *Environ. Prog. Sustain. Energy* **2012**, *31*, 536–543. [\[CrossRef\]](#)
- Kumar, A.; Kumar, J. On the synthesis and optical absorption studies of nano-size magnesium oxide powder. *J. Phys. Chem. Solids* **2008**, *69*, 2764–2772. [\[CrossRef\]](#)
- Veldurthi, S.; Shin, C.H.; Joo, O.S.; Jung, K.D. Synthesis of mesoporous MgO single crystals without templates. *Microporous Mesoporous Mater.* **2012**, *152*, 31–36. [\[CrossRef\]](#)

23. Zhao, Z.; Dai, H.; Du, Y.; Deng, J.; Zhang, L.; Shi, F. Solvo-or hydrothermal fabrication and excellent carbon dioxide adsorption behaviors of magnesium oxide with multiple morphologies and porous structures. *Mater. Chem. Phys.* **2011**, *128*, 348–356. [\[CrossRef\]](#)
24. Sundararajan, M.; Suresh, J.; Rajiv Gandhi, R. A comparative study on antibacterial properties of MgO nanoparticles prepared under different calcination temperature. *Dig. J. Nanomater. Biostruct.* **2012**, *7*, 983–989.
25. Athar, T.; Hakeem, A.; Ahmed, W. Synthesis of MgO nanopowder via non aqueous sol-gel method. *Adv. Sci. Lett.* **2012**, *7*, 27–29. [\[CrossRef\]](#)
26. Akbari, A.; Sabouri, Z.; Hosseini, H.A.; Hashemzadeh, A.; Khatami, M.; Darroudi, M. Effect of nickel oxide nanoparticles as a photocatalyst in dyes degradation and evaluation of effective parameters in their removal from aqueous environments. *Inorg. Chem. Commun.* **2020**, *115*, 107867. [\[CrossRef\]](#)
27. Sharma, N.; Kumar, J.; Thakur, S.; Sharma, S.; Shrivastava, V. Antibacterial study of silver doped zinc oxide nanoparticles against *Staphylococcus aureus* and *Bacillus subtilis*. *Drug Invent. Today* **2013**, *5*, 50–54. [\[CrossRef\]](#)
28. Hassan, S.M.; Ahmed, A.I.; Mannaa, M.A. Preparation and characterization of SnO₂ doped TiO₂ nanoparticles: Effect of phase changes on the photocatalytic and catalytic activity. *J. Sci. Adv. Mater. Devices* **2019**, *4*, 400–412. [\[CrossRef\]](#)
29. Khezrianjoo, S.; Lee, J.; Kim, K.-H.; Kumar, V. Eco-Toxicological and Kinetic Evaluation of TiO₂ and ZnO Nanophotocatalysts in Degradation of Organic Dye. *Catalysts* **2019**, *9*, 871. [\[CrossRef\]](#)
30. Wang, T.; Xu, Y.; Su, Q.; Yang, R.; Wang, L.; Liu, B.; Shen, S.; Jiang, G.; Chen, W.; Wang, S. Hierarchical porous nanosheet-assembled MgO microrods with high adsorption capacity. *Mater. Lett.* **2014**, *116*, 332–336. [\[CrossRef\]](#)
31. Slama, H.B.; Chenari, B.A.; Pourhassan, Z.; Alenezi, F.N.; Silini, A.; Cherif-Silini, H.; Oszako, T.; Luptakova, L.; Golińska, P.; Belbahri, L. Diversity of Synthetic Dyes from Textile Industries, Discharge Impacts and Treatment Methods. *Appl. Sci.* **2021**, *11*, 6255. [\[CrossRef\]](#)
32. Pradeep, K.; Ruchika, A.; Kailas, L.; Wasewar, H.U.; Yoo, C. Status of adsorptive removal of dye from textile industry effluent. *Desalination Water Treat.* **2012**, *50*, 226–244. [\[CrossRef\]](#)
33. Menon, P.; Singh, T.S.A.; Panic, N.; Nidheeshd, P.V. Electro-Fenton assisted sonication for removal of ammoniacal nitrogen and organic matter from dye intermediate industrial wastewater. *Chemosphere* **2021**, *269*, 128739. [\[CrossRef\]](#)
34. Lama, G.; Meijide, J.; Sanromán, A.; Pazos, M. Heterogeneous Advanced Oxidation Processes: Current Approaches for Wastewater Treatment. *Catalysts* **2022**, *12*, 344. [\[CrossRef\]](#)
35. Yaseen, D.A.; Scholz, M. Textile dye wastewater characteristics and constituents of synthetic effluents: A critical review. *Int. J. Environ. Sci. Technol.* **2019**, *16*, 1193–1226. [\[CrossRef\]](#)
36. Sergi, G.-S.; Enric, B. Applied photoelectrocatalysis on the degradation of organic pollutants in wastewaters. *J. Photochem. Photobiol. C Photochem. Rev.* **2017**, *31*, 1–35.
37. San, M.S.; Rivero, M.J.; Ortiz, I. Unravelling the Mechanisms that Drive the Performance of Photocatalytic Hydrogen Production. *Catalysts* **2020**, *10*, 901. [\[CrossRef\]](#)
38. Selvam, N.C.S.; Kumar, R.T.; Kennedy, L.J.; Vijaya, J.J. Comparative study of microwave and conventional methods for the preparation and optical properties of novel MgO- micro and nanostructures. *J. Alloys Compd.* **2011**, *509*, 9809–9815. [\[CrossRef\]](#)
39. Ansari, A.; Ali, A.; Asif, M. Shamsuzzaman, Microwave-assisted MgO NP catalyzed one-pot multicomponent synthesis of polysubstituted steroidal pyridines. *New J. Chem.* **2018**, *42*, 184–197. [\[CrossRef\]](#)
40. Nga, N.K.; Thuy, C.N.T.; Viet, P.H. Preparation and characterization of a chitosan/MgO composite for the effective removal of reactive blue 19 dye from aqueous solution. *J. Sci. Adv. Mater. Devices* **2020**, *5*, 65–72. [\[CrossRef\]](#)
41. Korbag, I.; Saleh, S.M. Studies on the formation of intermolecular interactions and structural characterization of polyvinyl alcohol/lignin film. *Int. J. Environ. Stud.* **2016**, *73*, 226–235. [\[CrossRef\]](#)
42. Karthik, K.; Dhanuskodi, S.; Gobinath, C.; Prabukumar, S.; Sivaramakrishnan, S. Fabrication of MgO nanostructures and its efficient photocatalytic, antibacterial and anticancer performance. *J. Photochem. Photobiol. B Biol.* **2019**, *190*, 8–20. [\[CrossRef\]](#)
43. Bindhu, M.R.; Umadevi, M.; Micheal, M.K.; Arasu, M.V.; Al-Dhabi, N.A. Structural, morphological and optical properties of MgO nanoparticles for antibacterial applications. *Mater. Lett.* **2016**, *166*, 19–22.
44. Hench, L.C.; West, J.K. *Principles of Electronic Ceramics*; John Wiley and Sons: New York, NY, USA, 1990.
45. Maoz, B.M.; Tirosh, E.; Sadan, M.B.; Markovich, G. Defect-induced magnetism in chemically synthesized nanoscale sheets of MgO. *Phys. Rev. B* **2011**, *83*, 161201. [\[CrossRef\]](#)
46. Gao, F.; Hua, J.; Yang, C.; Zheng, Y.; Qin, H.; Suna, L.; Konga, X.; Jiang, M. First-principles study of magnetism driven by intrinsic defects in MgO. *Solid State Commun.* **2009**, *149*, 855–858. [\[CrossRef\]](#)
47. Kumara, K.N.S.; Nagaswarupa, H.P.; Mahesh, K.R.V.; Prashantha, S.C.; Mylarappa, M.; Siddeshwara, D.M.K. Synthesis and characterization of nano ZnO and MgO powder by low temperature solution combustion method: Studies concerning electrochemical and photocatalytic behavior. *Nanosyst. Phys. Chem. Math.* **2016**, *7*, 662–666. [\[CrossRef\]](#)
48. Jain, U.; Pundir, C.S.; Gupta, S.; Chauhan, N. A novel electrochemical comparative sensing interface of MgO nanoparticles synthesized by different methods. *Proc. Inst. Mech. Eng. Part C J. Mech. Eng. Sci.* **2017**, *233*, 753–762. [\[CrossRef\]](#)
49. Mathialagan, A.; Manavalan, M.; Venkatachalam, K.; Mohammad, F.; Oh, W.C.; Sagadevan, S. Fabrication and physicochemical characterization of g-C₃N₄/ZnO composite with enhanced photocatalytic activity under visible light. *Opt. Mater.* **2020**, *100*, 109643. [\[CrossRef\]](#)

50. Muthukumaran, M.; Prasath, P.V.; Kulandaivelu, R.; Sagadevan, S.; Mohammad, F.; Oh, W.C. Fabrication of nitrogen-rich graphitic carbon nitride/Cu₂O (gC₃N₄@Cu₂O) composite and its enhanced photocatalytic activity for organic pollutants degradation. *J. Mater. Sci. Mater. Electron.* **2020**, *31*, 2257–2268. [[CrossRef](#)]
51. Balakrishnan, G.; Velavan, R.; Batoo, K.M.; Emad; Raslan, H. Microstructure, optical and photocatalytic properties of MgO nanoparticles. *Results Phys.* **2020**, *16*, 103013. [[CrossRef](#)]
52. Kumar, M.R.A.; Mahendra, B.; Nagaswarupa, H.P.; Surendra, B.S.; Ravikumar, C.R.; Shetty, K. Photocatalytic Studies of MgO Nano Powder; Synthesized by Green Mediated Route. *Mater. Today: Proc.* **2018**, *5*, 22221–22228.
53. Bagheri GH, A.; Sabbaghanb, M.; Mirgani, Z. A comparative study on properties of synthesized MgO with different templates. *Spectrochim. Acta Part A Mol. Biomol. Spectrosc.* **2015**, *137*, 1286–1291. [[CrossRef](#)]
54. Khan, M.I.; Akhtar, M.N.; Ashraf, N.; Najeeb, J.; Munir, H.; Awan, T.I.; Tahir, M.B.; Kabli, M.R. Green synthesis of magnesium oxide nanoparticles using Dalbergia sissoo extract for photocatalytic activity and antibacterial efficacy. *Appl. Nanosci.* **2020**, *10*, 2351–2364. [[CrossRef](#)]
55. Alaizeri, Z.M.; Alhadlaq, H.A.; Aldawood, S.; Akhtar, M.J.; Amer, M.S.; Ahamed, M. Facile Synthesis, Characterization, Photocatalytic Activity, and Cytotoxicity of Ag-Doped MgO Nanoparticles. *Nanomaterials* **2021**, *11*, 2915. [[CrossRef](#)]